A Comparison of Scan Speedup Strategies and Their Effect on Rapid-Scan Weather Radar Data Quality

ANDREW MAHRE,[a,b] TIAN-YOU YU,[c,b,a] AND DAVID J. BODINE[b,a]

[a] School of Meteorology, University of Oklahoma, Norman, Oklahoma; [b] Advanced Radar Research Center, University of Oklahoma, Norman, Oklahoma; [c] School of Electrical and Computer Engineering, University of Oklahoma, Norman, Oklahoma

ABSTRACT: As the existing NEXRAD network nears the end of its life cycle, intense study and planning are underway to design a viable replacement system. Ideally, such a system would offer improved temporal resolution compared to NEXRAD, without a loss in data quality. In this study, scan speedup techniques—such as beam multiplexing (BMX) and radar imaging—are tested to assess their viability in obtaining high-quality rapid updates for a simulated long-range weather radar. The results of this study—which uses a Weather Research and Forecasting (WRF) Model–simulated supercell case—show that BMX generally improves data quality for a given scan time or can provide a speedup factor of 1.69–2.85 compared to NEXRAD while maintaining the same level of data quality. Additionally, radar imaging is shown to improve data quality and/or decrease scan time when selectively used; however, deleterious effects are observed when imaging is used in regions with sharp reflectivity gradients parallel to the beam spoiling direction. Consideration must be given to the subsequent loss of sensitivity and beam broadening. Finally, imaging is shown to have an effect on the radar-derived mesocyclone strength (ΔV) of a simulated supercell. Because BMX and radar imaging are most easily achieved with an all-digital phased array radar (PAR), these results make a strong argument for the use of all-digital PAR for high-resolution weather observations. It is believed that the results from this study can inform decisions about possible scanning strategies and design of a NEXRAD replacement system for high-resolution weather radar data.

KEYWORDS: Data quality control; Radars/Radar observations; Error analysis

1. Introduction

For the next-generation phased array radar (NexPAR) network for high-resolution weather observations in the United States, a primary goal is to improve temporal resolution (to ~1 min) with respect to the current ~5-min update time offered by the current national network of Weather Surveillance Radar-1988 Doppler (WSR-88D) radars (Weber et al. 2019). While the deployment of WSR-88Ds [also called Next-Generation Weather Radar (NEXRAD)] and subsequent technology upgrades have improved severe weather warning performance and lead times (Polger et al. 1994; National Research Council 1995; Bieringer and Ray 1996; Simmons and Sutter 2005), many observations of weather phenomena require even faster update times. Further, the limitations of the current NEXRAD system may be contributing to the observed plateau in tornado warning performance and lead times in recent years (Brooks and Correia 2018); this further emphasizes the need for improved observing technology. The primary reason why rapid-scanning radar is necessary in meteorology is that many weather phenomena evolve on the order of tens of seconds or less, rather than on the order of several minutes (e.g., Carbone et al. 1985; Wolfson and Meuse 1993; French et al. 2013; Wurman and Kosiba 2013; French et al. 2014; Houser et al. 2015; Wakimoto et al. 2015; Kurdzo et al. 2017; Mahre et al. 2017, 2018; Bluestein et al. 2019; Griffin et al. 2019). For forecasting and operational purposes, Heinselman et al. (2012) and Wilson et al. (2017) have shown that the introduction of rapid scans with a phased array radar (PAR) leads to increased warning lead time, improved forecaster

confidence, a higher probability of detection, and a lower false alarm ratio for tornadoes in a simulated operational setting. Additionally, data assimilation studies have shown the benefit of assimilating rapid-scan weather radar data to improve short-term numerical weather prediction (NWP) model accuracy (Yussouf and Stensrud 2010; Sun et al. 2014; Supinie et al. 2017). In practice, however, consideration must be given to the fact that improvements in update time often come at the expense of degraded data quality or reduced total coverage volume (Heinselman and Torres 2011). Hereinafter, ''data quality'' is used to refer to expected errors from statistical variance in radar variables as well as possible biases, as these generally present some of the largest sources of possible detriments to the usability of data for forecasters (Doviak and Zrnić 1993). An attempt to scan faster simply by decreasing dwell time per radial (e.g., rotating the radar dish faster in a nonphased array system) will result in deleterious effects on data quality, if all other scan parameters are held constant.

One major factor that significantly impacts data quality is the radar design and architecture. While it is likely that a NEXRAD replacement network will utilize phased array technology, the aperture size, transmit power, and scanning mode (mechanical or electronic) are still undetermined (Weber et al. 2019). Additionally, the desired missions of the radar system (i.e., multifunction or weather only) will determine the scan timeline percentage that can be devoted to weather observations. Because of these system and network uncertainties, this study intends to investigate a representative subset of the possible radar architectures of the final system [e.g., PD-3 and PD-4 in Weber and Herd (2019), which are notional 6–7-m-diameter high-resolution weather radars that are possible designs for a NexPAR system] using simulations, rather than attempting to

account for all possible design architectures. Additionally, this study only analyzes data quality impact on horizontal reflectivity factor (Z_H) and radial velocity (v_r), as they are important nonpolarimetric radar variables for operational forecasters. Polarimetric variables are not considered in this study, because polarimetric biases and considerations from radar architecture and system design could play a larger role in overall polarimetric data quality than statistical fluctuations. However, we propose studying polarimetric statistical fluctuations as a possible future route of research. The conclusions herein are intended to provide a general framework for a discussion of the advantages and disadvantages of various scan techniques and radar design architectures.

Speeding up a scan simply by reducing the number of samples per radial will inevitably reduce data quality (Doviak and Zrnić 1993; Yu et al. 2007; Reinoso-Rondinel et al. 2010). This presents an obvious challenge when considering that an overall scan speedup of 1.25–5 times is desired for NexPAR compared to NEXRAD, in order to achieve the NexPAR goal of 1-min volumetric updates (Weber et al. 2017, 2019). Thus, to achieve acceptable data quality—where "acceptability" is defined by the system performance requirements, such as 1 dBZ or 1 m s^{-1} for reflectivity factor and radial velocity, respectively—other scan methods will need to be employed. A few possible methods through which data quality can be maintained in a rapid-scan phased array weather radar include

- radar imaging and digital beamforming (e.g., Isom et al. 2013), where the transmit beam is spoiled in azimuth and/or elevation in order to cover a larger area simultaneously at the expense of higher two-way sidelobes, lowered sensitivity, and a broader mainlobe, while digital beamforming (DBF) is used on receive to electronically form narrow, individual receive beams;
- beam multiplexing (BMX; Yu et al. 2007), where successive transmit pulse pairs are steered in different directions before returning to the original transmit direction in order to allow for more decorrelation of the received signals, increasing the number of independent samples per unit scan time; drawbacks include a lack of support for ground-clutter filtering and staggered pulse repetition time (staggered PRT) processing;
- multiple-beam technique (MBT; Zrnić et al. 2015; Melnikov et al. 2015), where N beams ($N > 1$) are transmitted in N directions in rapid succession, using digital beamforming on receive;
- adaptive scanning (e.g., Reinoso-Rondinel et al. 2010; Heinselman and Torres 2011), where the beam is electronically steered toward areas of interest and away from areas not of interest to the user.

In this study, adaptive scanning techniques such as Automated Volume Scan Evaluation and Termination (AVSET) (Chrisman 2009) or Adaptive Digital Signal Processing Algorithm for PAR Timely Scans (ADAPTS) (Heinselman and Torres 2011) are not considered, as they are beyond the scope of this paper. For future studies, adaptive use of BMX (e.g., only using BMX at higher elevation angles or in situations where minimal ground clutter is present) could be a promising compromise to mitigating the ground clutter filtering drawback. Herein, the

TABLE 1. A list of the WRF Model parameterizations used in this study.

Parameterization type	Parameterization name
Microphysics scheme	Morrison
Land surface scheme	Noah (Chen and Dudhia 2001)
Cumulus parameterization	Kain–Fritsch (at 27- and 9-km grids)
PBL scheme	Yonsei University (YSU; Hong et al. 2006)
Longwave radiation scheme	RRTM (Mlawer et al. 1997)
Shortwave radiation scheme	Dudhia (Dudhia 1989)

comparison of results based on volume coverage pattern (VCP) and scanning strategy selection (i.e., radar imaging and BMX) offers insights into the effects of adaptive scanning on operational radar data quality and hazard detection algorithms.

The purpose of this study is to quantify the effects of various scanning strategies on radar data quality by using Radar Simulator (RSim), a new, flexible dual-polarization radar emulator that has been developed by the University of Oklahoma Advanced Radar Research Center (OU ARRC). This study is novel in that it quantifies and compares data quality from multiple scanning strategies and data collection methods for a large area, allowing for a direct comparison of data quality between scanning strategies. Finally, the effect of radar imaging on the estimate of mesocyclone intensity is shown for the first time. While it has previously been shown that changing the effective beamwidth of the radar by altering the azimuthal sampling can affect tornado detection capability (e.g., Brown et al. 2002), this is the first study to research the effect of changing the radar transmit pattern on rotation intensity measurements/estimates.

This study is the first to use a large-scale radar simulator with realistic weather inputs for data quality assessment; this method offers multiple advantages over other methods. First, it allows for assessment of data quality for a realistic case (a simulated supercell in the 31 May 2013 central Oklahoma environment; Wurman et al. 2014; Wakimoto et al. 2015, 2016; Tanamachi and Heinselman 2016; Bluestein et al. 2018, 2019). This case was chosen because data quality is especially important for high-impact events where significant life and property are lost and accurate forecasts are imperative. This method offers insight into the full distribution of data quality over a large area and accounting for the spatial distribution of spectrum width and signal-to-noise ratio (SNR) and any dependence between these two variables. Second, such comparisons are only achievable with a large-scale radar simulator (rather than an actual radar system) because the same simulated thunderstorm is used for each case, enabling direct comparisons. Third, RSim uses model data that are output from WRF at 1-min intervals (i.e., 1-min temporal resolution); this offers advantages compared to simulators that use data with coarser temporal resolution as their basis. The reason why using rapidly updating model data is advantageous is that the update time of the microphysical and velocity fields is on the order of the full volumetric update time. As such, no assumptions need to be made about vertical advection or temporal–spatial interpolation between scans.
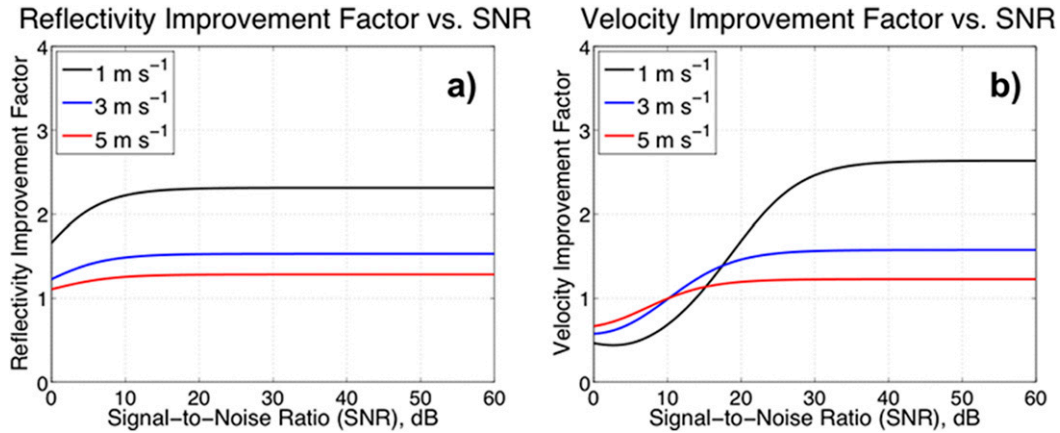
FIG. 1. Improvement factor for (a) Z_H and (b) v_r as a function of SNR using BMX. The three lines represent spectrum width of 1 (black line), 3 (blue line), and 5 m s^{-1} (red line).

The results from this study are novel and expand upon previous studies such as Yu et al. (2007) and Weber et al. (2017). For example, the achievable scan speedup factor with BMX is calculated using simulated radar data quality over a large area and at multiple times and several elevation angles, as opposed to calculating data quality over a small area or along one radial (e.g., Fig. 5 and Fig. 7 of Yu et al. 2007). This should yield a more accurate estimate of speedup factor for a NexPAR-style system. Additionally, this paper focuses on the entire histogram of data quality estimates, rather than simply calculating the number of pixels which have "unacceptable" data quality estimates, such as in Weber et al. (2017).

Many of the scan speedup techniques tested in this study are only easily achievable with a fully flexible, all-digital phased array radar architecture (e.g., Palmer et al. 2019). The conclusions on error estimation and data quality can help determine which scanning strategies are viable for achieving full-volume updates on the order of 1 min without sacrificing data quality. The results herein should be applicable to a wide range of NexPAR designs (four-faced stationary PAR, one-faced mechanically rotating PAR, etc.).

In this study, data quality is estimated from a simulated rapid-scan weather radar by comparing expected RMSE of radar variables. Data quality is then compared between multiple scan scenarios, where various methods are employed to achieve faster PPI scans. Comparisons of data quality include 1) altering the number of pulses per radial, 2) BMX and non-BMX data collection modes, and 3) varying levels of transmit beam spoiling with DBF on receive (i.e., imaging).

2. Methods

a. RSim

For the analysis conducted herein, a radar simulator is used. Simulators can reveal important information regarding the expected fields from a number of controlled input scenarios and allow for direct comparison of data quality between scan methods because of the ability to reanalyze the same simulated weather event with different scanning strategies. Of course,

there are limitations of radar simulators; for example, features such as ground clutter and nonhydrometeor scatterers are not simulated. As a result, it is useful to verify these results with a real-world radar system. This study utilizes output from RSim in order to assess and quantify the data quality of a rapid-scan weather radar system.

In this study, multiple assumptions are made regarding the radar specifications. For example, polarimetric biases are not considered; a relative lack of polarimetric bias would be consistent with a single-faced, mechanically rotating PAR or a cylindrical PAR (Zhang et al. 2011). Furthermore, the beamwidth and antenna gain are assumed to be constant throughout the PPI, which would also be consistent with the previously mentioned radar types, assuming that the maximum beamsteering angle (relative to broadside) is not too large. Finally, the noise floor is assumed to be the same as that of a WSR-88D (-7.5 dBZ at 50 km in range) in order to facilitate comparisons to NEXRAD.

RSim uses WRF Model data (Skamarock et al. 2008) as input and computes moment data (i.e., reflectivity factor, radial velocity, and spectrum width) in the radar domain based on the number concentration and radial velocity of each hydrometeor type at each model grid point. RSim uses T-matrix scattering for four hydrometeor types: rain, graupel, snow, and ice. The T-matrix method relates scattering amplitudes to the particle size distribution (PSD) for each hydrometeor type (Mishchenko et al. 1996; Mishchenko 2000). More information about the T-matrix scattering method and polarimetric variable estimation

TABLE 2. A summary of the SENSR PPR for reflectivity factor, radial velocity, and spectrum width maximum standard deviation for a specified SNR and true spectrum width (σ_v).

	SNR	σ_v	Standard deviation requirement
Z_H	>10 dB	4 m s^{-1}	<1 dBZ
v_r	>8 dB	4 m s^{-1}	<1 m s^{-1}
σ_v	>10 dB	4 m s^{-1}	<1 m s^{-1}

Reference Fields (1° Elevation, 20 s per PPI)

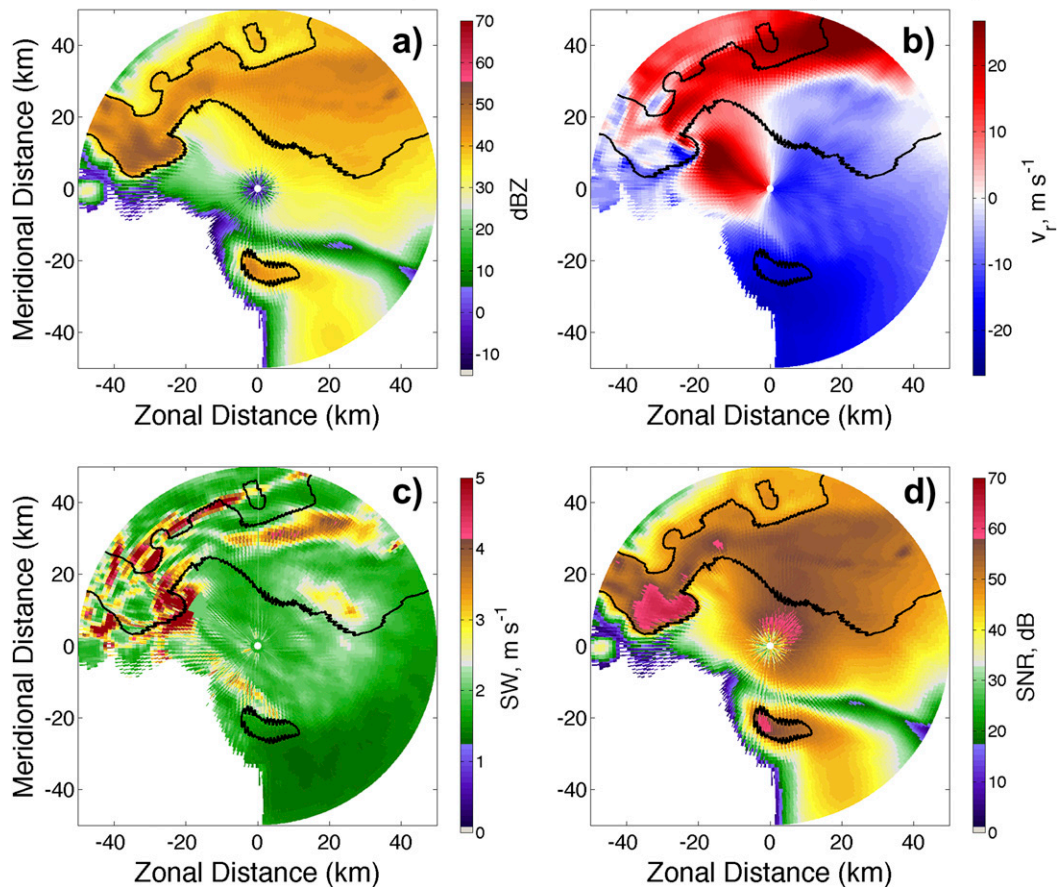
FIG. 2. PPIs showing (a) horizontal reflectivity factor (Z_H, in dBZ), (b) radial velocity (in m s^{-1}), (c) estimated spectrum width (in m s^{-1}), and (d) signal-to-noise ratio (SNR; in dB). All PPIs are shown at 0124:00 UTC. Mean spectrum width is 2.48 m s^{-1}. The black contour corresponds to 38 dBZ.

can be found in Zhang et al. (2001) and Jung et al. (2008). The radar emulations derived through RSim account for angular and range weighting functions, by weighting the microphysical contributions at each model grid point based on the range and antenna weighting patterns. Each model grid point in RSim is weighted and summed to derive the expected moments at each azimuth, elevation, and range combination in the radar scan domain. Range weighting patterns and antenna beam patterns (proportional to sinc$^2 r$ and sinc$^2\theta$ sinc$^2\phi$, respectively) used in this study are based on established patterns in Doviak and Zrnić (1993) and Orfanidis (2016), where r is the range, θ is the azimuth angle, and ϕ is the elevation angle. RSim provides significant scanning flexibility, in that radar imaging can be simulated using spoiled beams on transmit and pencil beams on receive; nonsequential beam positions can also be simulated.

For this study, the model parameterizations used for WRF are identical to those used in Bodine and Rasmussen (2017); the parameterizations are listed in Table 1. Two-way nesting is used between the grids and 0.25° Global Forecast System

(GFS) data are used to initialize the simulations. Additionally, 44 vertical grid points are used with finest vertical grid spacing in the boundary layer. WRF was run at 1-km horizontal grid spacing and 1-min temporal resolution for a supercell in the 31 May 2013 central Oklahoma environment; larger 27-, 9-, and 3-km domains are used outside this innermost mesh to

TABLE 3. A list of RSim scan parameters used in this study.

Scan parameter	Value(s)
Scan times	0124, 0126, 0128, 0130, and 0132 UTC
Elevation angles	0.5°, 4.0°, and 8.0°
Radar wavelength	0.107 m
PRT	1 ms
Range resolution and sampling	1 km
Azimuthal sampling	0.5°
Noise floor	−7.5 dBZ at 50 km
SNR threshold	3 dB

TABLE 4. A summary of the scanning strategies assessed in this study.

Scan technique name	Time per PPI	Data collection mode	Azimuthal beamwidth
NEXRAD-style scan	20 s	CPS	1°
10-s scan	10 s	CPS	1°
BMX scan	20 s	BMX (IPS)	1°
Radar imaging scan	20 s	CPS	10°

downscale from larger-scale conditions. The model started at 0000 UTC 31 May 2013, such that the supercell of interest for this case is analyzed approximately 25.5 h after the start of the model.

To estimate spectrum width, local thermodynamic data and radial velocity estimates are used. While the contribution of larger-scale shear on spectrum width can be estimated as the local standard deviation of velocity (σ_s; Doviak and Zrnić 1993), this does not capture smaller-scale

turbulence, which has a significant contribution to the overall spectrum width of the resolution volume (Brewster and Zrnić 1986; Doviak and Zrnić 1993; Nastrom and Eaton 1997; Zhang et al. 2009). The overall spectrum width can be estimated as

$$\sigma_v^2 = \sigma_s^2 + \sigma_t^2, \tag{1}$$

where σ_v is the spectrum width observed by the radar and σ_t is the turbulence contribution. Other contributions to spectrum width, such as antenna motion, hydrometeor vibrations, and differential hydrometeor fall speeds are ignored as these do not have as large of a contribution as the shear and turbulence terms (Brewster and Zrnić 1986; Zhang et al. 2009). With the shear contribution being estimated by the local spatial standard deviation of velocity (Doviak and Zrnić 1993), the turbulence contribution can be estimated by using a rearranged version of Eq. (2) from Nastrom and Eaton (1997):
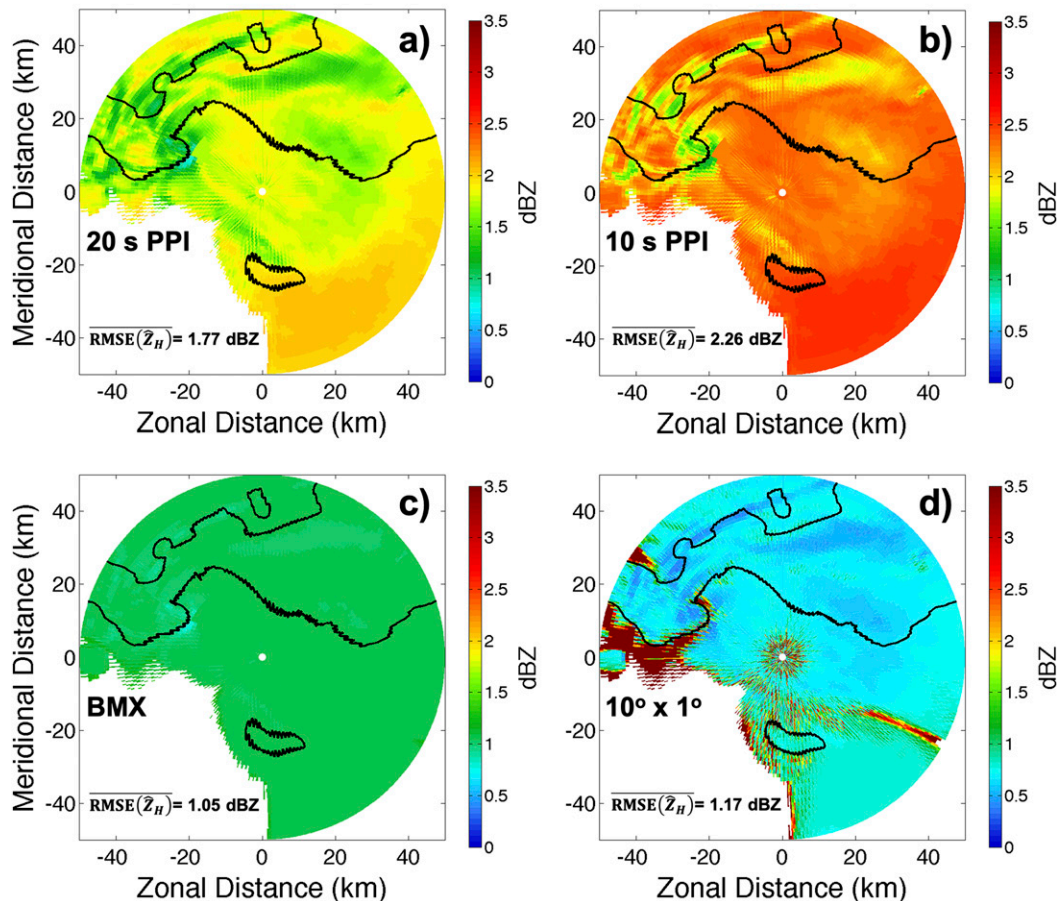

FIG. 3. PPIs showing the calculated RMSE of Z_H for (a) a pencil beam using CPS with a scan time of 20 s per PPI, (b) a pencil beam using CPS with a scan time of 10 s per PPI, (c) a pencil beam using BMX (IPS) with a scan time of 20 s per PPI, and (d) a 10° fan beam using CPS with a scan time of 20 s per PPI. All PPIs are at 0124:00 UTC, at 0.5° in elevation.

$$\sigma_t^2 = \frac{\varepsilon A^{3/2}}{f_{BV}}, \qquad (2)$$

where ε is the turbulent eddy dissipation rate, $A = 1.6$ is the Kolmogorov constant, and f_{BV} is the Brunt–Väisälä frequency, where $f_{BV} = \sqrt{(g/\theta)(d\theta/dz)}$, g is gravitational acceleration, and $d\theta/dz$ is the vertical gradient of potential temperature, where θ is potential temperature and z is the vertical coordinate. The turbulent eddy dissipation rate used in this study is $0.02\,\mathrm{m^2\,s^{-3}}$; this is lower than in most literature sources [0.06 or $0.10\,\mathrm{m^2\,s^{-3}}$ in Frisch and Strauch (1976) and Doviak and Zrnić (1993), respectively]. However, the value of $0.02\,\mathrm{m^2\,s^{-3}}$ is used in this study to produce spectrum width values that are consistent with NEXRAD observations (Fang et al. 2004). Brunt–Väisälä frequency is estimated using thermodynamic data from each grid point in the WRF domain.

b. Data quality

For the purposes of this study, data quality is defined as the expected RMSE of radar variables in question. For signal power and radial velocity estimates from non-BMX data collection mode [also called contiguous pulse sampling (CPS)] and a pulse-pair processor, the variance of the signal power and velocity estimators are given by Zrnić (1977), Doviak and Zrnić (1993), and Yu et al. (2007):

$$\frac{\mathrm{var}(\hat{S}_C)}{S^2} = \frac{1}{D+1}\left[\sum_{l=-D}^{D}\frac{D-|l|+1}{D+1}\rho^2(lT_s) + \frac{N^2}{S^2} + 2\frac{N}{S}\right], \qquad (3)$$

$$\mathrm{var}(\hat{v}_C) = \frac{\lambda^2}{32\pi^2 D\rho^2(T_s)T_s^2}\left\{[1-\rho^2(T_s)]\sum_{l=-(D-1)}^{D-1}\frac{D-|l|}{D}\rho^2(lT_s)\right.$$

$$\left. + \frac{N^2}{S^2} + 2\frac{N}{S}\left[1 - \frac{D-1}{D}\rho(2T_s)\right]\right\}, \qquad (4)$$

where λ is the radar wavelength, D is the number of pulse pairs (equal to the number of pulses minus one for contiguous pulse pairs), T_s is the pulse repetition time (PRT), ρ is the signal normalized autocorrelation function, S is the signal power, N is the noise power, and $\hat{S}_C$ and $\hat{v}_C$ are the estimators for signal power and radial velocity in CPS mode, respectively. The signal power S (and by extension SNR) is derived from the Z_H calculated from the forward operator. The signal normalized correlation between samples as a function of time, $\rho(T)$, is given by Doviak and Zrnić (1993):

$$\rho(dT_s) = \exp\left[-8(\pi\sigma_v dT_s/\lambda)^2\right], \quad \text{where} \quad d = 0,1,2,\ldots,D, \qquad (5)$$

where σ_v is the spectrum width and d is equal to the (integer) number of PRTs between two pulses.

For BMX applications [also called independent pulse sampling (IPS)], in which pulse pairs are independent rather than contiguous, the variance of the signal power and velocity estimators reduce to the following equations from Yu et al. (2007):
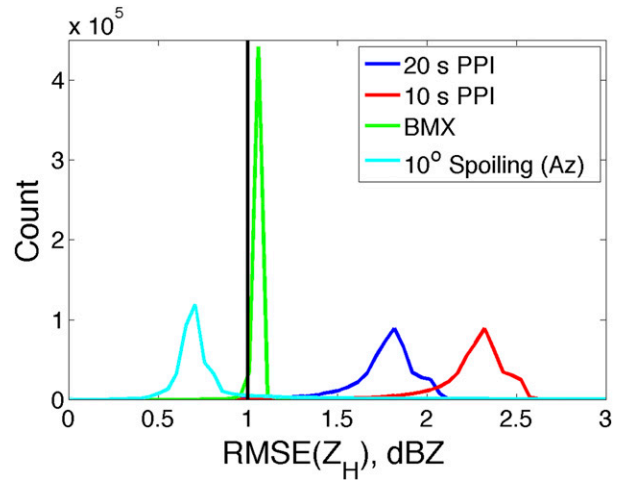

FIG. 4. Histogram of mean Z_H RMSE estimates at five times and three elevation angles (0.5°, 4.0°, and 8.0°). The black vertical line represents the 1-dBZ suggested requirement (see Table 2).

$$\frac{\mathrm{var}(\hat{S}_I)}{S^2} = \frac{1}{2L}\left[1 + \rho^2(T_s) + \frac{N^2}{S^2} + 2\frac{N}{S}\right], \qquad (6)$$

$$\mathrm{var}(\hat{v}_I) = \frac{\lambda^2}{32\pi^2 L\rho^2(T_s)T_s^2}\left[1 - \rho^2(T_s) + \frac{N^2}{S^2} + 2\frac{N}{S}\right], \qquad (7)$$

where $\hat{S}_I$ is the power estimate when using BMX data collection mode and L is the number of pulse pairs, equal to the number of total pulses divided by two in BMX data collection mode. To obtain the standard deviation of reflectivity factor, the following equation is used:

$$\mathrm{SD}(\hat{Z}_H) = 10\log_{10}\left[1 + \frac{\mathrm{SD}(\hat{S})}{S}\right], \qquad (8)$$

where $\mathrm{SD}(\hat{Z}_H)$ is the standard deviation of horizontal reflectivity factor. For this study, RMSE is calculated as follows:

$$\mathrm{RMSE}(\hat{X}) = \sqrt{\mathrm{SD}(\hat{X})^2 + (\hat{X} - X_{\mathrm{ref}})^2}, \qquad (9)$$

where $\hat{X}$ is the estimated radar variable, SD stands for standard deviation, and X_{ref} is the value of X in the reference field, such that RMSE is equal to the square root of the statistical fluctuation squared (i.e., the variance of the estimator) plus the bias (relative to the reference field) squared. Note that this definition of bias is not the statistical definition of a biased estimator. Rather, it is intended to compare the difference between a "baseline" scan truth value and the "new" truth value. For all scanning strategies except for radar imaging, the bias values are assumed to be zero, such that the RMSE is equal to the standard deviation(s) calculated in (3)–(8).

In practical weather applications, moment variance depends on 1) the number of pulses or pulse pairs, 2) spectrum width, and 3) SNR, defined as S/N. Additionally, data collection mode (BMX vs CPS) affects moment variance by changing the equation(s) used. The number of pulses per radial and data
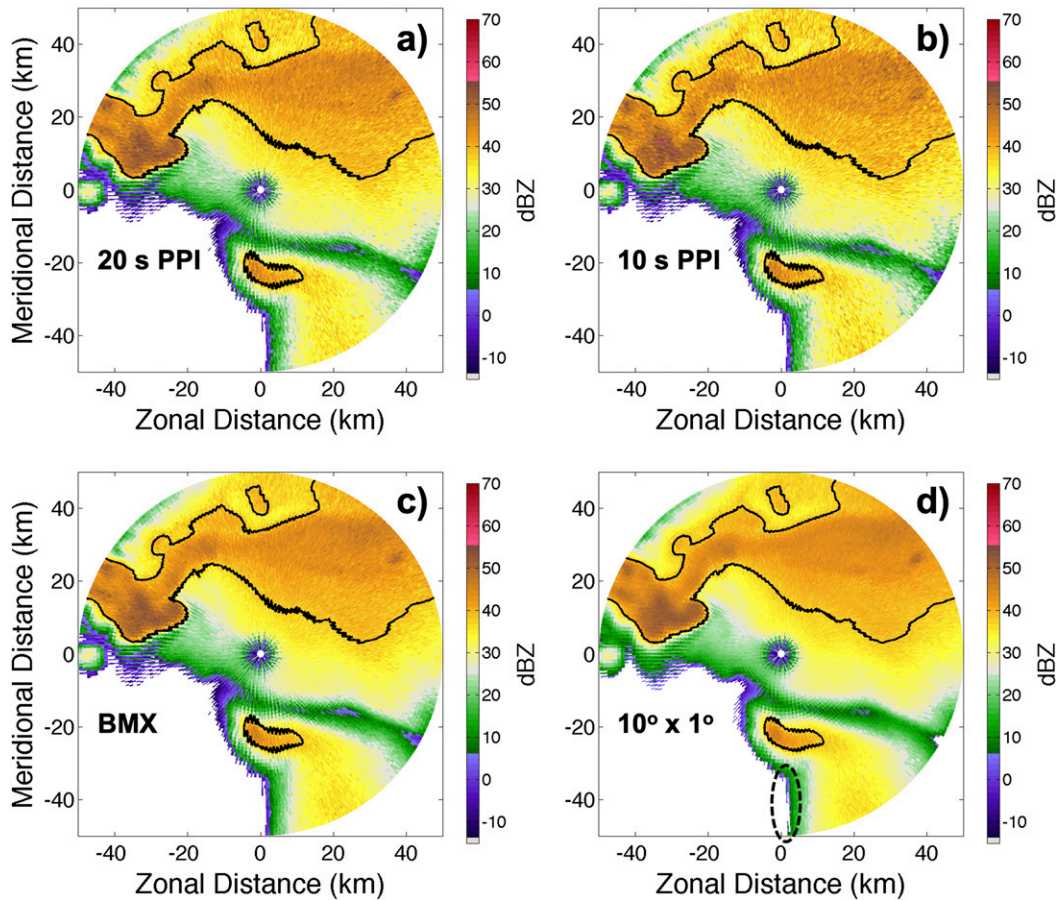
Reflectivity Factor (Z_H)

FIG. 5. PPIs showing the reference Z_H fields with the expected standard deviation added as additive white Gaussian noise (AWGN) for (a) a 20-s PPI, (b) a 10-s PPI, (c) BMX data collection mode, and (d) an azimuthally spoiled beam. Note that the underlying reference field is different in (d) due to the lowered sensitivity (e.g., dashed circled region) and higher antenna sidelobes.

collection mode are the variables over which the radar operator has control, through VCP and scanning strategy design. In BMX, the number of pulse pairs for velocity estimation is reduced by a factor of $D/L = (M − 1)/(M/2) = 2 − 2/M$ compared to CPS, where M is the number of pulses along each radial. Thus, it is possible for velocity estimates to worsen, especially in areas of high spectrum width and/or low SNR (e.g., Fig. 4b in Yu et al. 2007) due to the decrease in the number of pulse pairs. Figure 1 shows a plot of both reflectivity and velocity improvement factor as a function of SNR for three values of spectrum width, where reflectivity (velocity) improvement factor is defined as the ratio between expected statistical standard deviation of Z_H (v_r) using CPS [(3), (4)] divided by the statistical standard deviation of Z_H (v_r) using BMX [(6), (7)]. At low SNR, generally less than 10–15 dB, improvement factor is less than 1 for v_r, indicating that CPS yields better velocity estimates compared to BMX. Also, the improvement factor reaches a different asymptote at high SNR

for each spectrum width value. For the high spectrum width case, the improvement factor at high SNR for Z_H (v_r) generally does not exceed 1.28 (1.23). Thus, the improvement in data quality by using BMX is very limited for high spectrum width. However, it should be noted that under no circumstances is RMSE for Z_H or differential reflectivity factor (Z_{DR}) negatively affected by using BMX instead of CPS. This is because the number of reflectivity factor samples is the same between BMX and CPS modes, while the increased sample independence can only improve the reflectivity factor estimates for BMX mode compared to CPS mode.

For the data quality requirements used in this study, the preliminary program requirements (PPR) for the Spectrum Efficient National Surveillance Radar (SENSR) program are used (Federal Aviation Administration 2017), which are similar to current NEXRAD data requirements. The SENSR requirements are used because SENSR was, at the time of its design, planned to be the rapid-scan weather radar system to

replace NEXRAD. A summary of the data quality requirements in the PPR is given in Table 2. For this study, the $1\,\mathrm{m\,s^{-1}}$ velocity RMSE requirement and the 1 dBZ reflectivity RMSE requirement are used for expected data quality in a rapid-scan system, although the final NexPAR design may alter the data quality requirements listed in Table 2. This study will focus on the effect of scanning strategies on the expected RMSE of the Z_H and v_r estimators, as well as the effect of radar imaging on mesocyclone intensity observations.

3. Results

a. Data quality and error estimation

In this section, RSim is used to examine expected RMSE of radar variables in a supercell case. The supercell case in this study uses a WRF simulation from 31 May 2013 in central Oklahoma. Radar returns are simulated with various scan modes. Errors for the scan modes are estimated by using (3)–(8). This analysis is performed on 15 PPIs: 0124, 0126, 0128, 0130, and 0132 UTC at 0.5°, 4.0°, and 8.0° in elevation. PPIs of relevant radar variables at 0124 UTC are shown in Fig. 2.

The selected times and heights were chosen to capture multiple times where the tornado was near its strongest intensity; the elevations were chosen to sample near 250 m, 2 km, and 4 km AGL. The simulated radar has a beamwidth of 1°, oversampled to 0.5° in azimuth. The data shown are thresholded at 3 dB of SNR and a range resolution of 1 km is assumed. While this range resolution is coarser than NEXRAD, it should be noted that this range resolution is constant across all cases studied herein, such that comparisons should hold at any realistic range resolution. A list of relevant RSim scan parameters are shown in Table 3.

For an estimation of expected RMSE, several assumptions are made regarding the radar system. Representative parameters for a notional NexPAR system are used as inputs into RSim; for example, a radar wavelength of 0.107 m is used with a similar noise floor estimate (-7.5 dBZ at 50 km) to that of NEXRAD. Here, a relatively short (1 ms) PRT is used to simulate a "velocity cut" in NEXRAD. These values are used as input into (3)–(7), along with the PPIs of SNR and spectrum width at a given time, to generate a PPI of signal power, reflectivity factor, and velocity error estimates in both BMX and CPS data collection modes. Holding these system parameters constant, it is then possible to alter the scanning strategy to assess the data quality impact on each radar variable of interest.

1) RADAR REFLECTIVITY FACTOR (Z_H)

First, this study will analyze the effect of scanning strategy choice on data quality for Z_H. A summary of the scanning strategies tested in section 3a is given in Table 4. Data quality is assessed by using (3), (6), and (8), where the scanning strategies used are described below. Different scanning strategies are used to assess the impact on data quality and calculate any possible scan speedup, where scan speedup is the ability to complete a scan more quickly while maintaining the same level of data quality. Figure 3 shows the RMSE of $\hat{Z}_H$—calculated
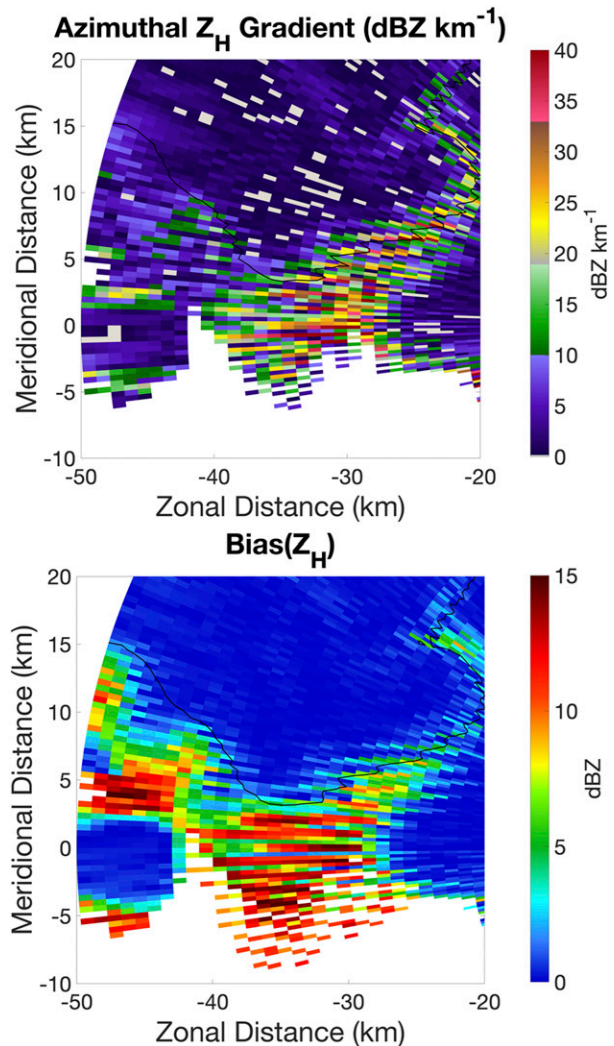

FIG. 6. A comparison of (top) the measured horizontal gradient in Z_H with (bottom) the bias of Z_H between the pencil beam method and a scan with 10° of azimuthal beam spoiling.

using (9)—under four scanning strategies, analyzed at one time (0124 UTC 31 May 2013) and one elevation angle (0.5°). Figure 3a is a NEXRAD-style "reference" scan, to which the other data collection techniques are compared. This NEXRAD-style scan transmits a "pencil beam" (1° × 1°), collects a full PPI in 20 s (similar to the low-level scan rate in VCP 215), and uses CPS data collection mode. The data collection strategy in Fig. 3b is identical to the technique in Fig. 3a, except that the time to complete the PPI is decreased from 20 to 10 s by reducing the number of samples per radial; this results in a subsequent degradation in data quality (i.e., RMSE increases). Figure 3c transmits a pencil beam with a scan time of 20 s but uses BMX data collection mode rather than CPS data collection mode. The BMX mode scan assumes a 20-s scan where successive pulse pairs are transmitted along different radials, such that each pulse pair is independent; the total number of pulses remains constant with the reference, NEXRAD-style
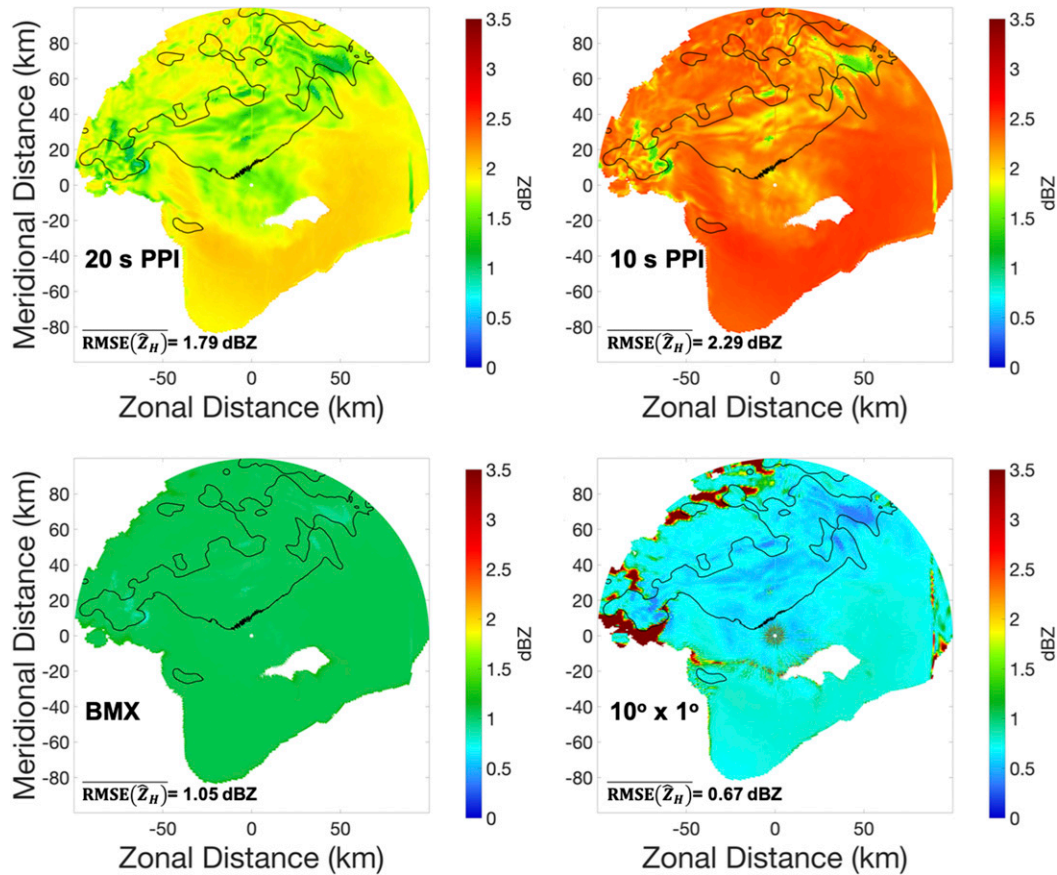
RMSE(Z_H)

FIG. 7. As in Fig. 3, but for a longer radar standoff range ($\sim$60 km to the mesocyclone).

scan in Fig. 3a. In Fig. 3d, radar imaging (10° in azimuth) is used with a scan time of 20 s while mechanically rotating the radar in azimuth; this has the effect of increasing the number of samples per radial at the expense of higher two-way antenna sidelobes in azimuth. Note that because the reference fields for Figs. 3a–c are identical, the RMSE plotted in Figs. 3a–c is simply equal to the statistical standard deviation.

To achieve rapid scans for a weather radar system, the most straightforward method is to decrease the number of samples along each radial (assuming a constant PRT). This decreases the number of pulses available for moment estimation [i.e., a decrease in D in (3) and (4) and a decrease in L in (6) and (7)]. For a mechanically rotating radar system, this could correspond to an increased rotation rate of the antenna. For a stationary (electronically scanning) system, such a change could come as the result of changing from a weather-only radar system to a multifunction system.

To examine these errors with a larger sample size of data, mean RMSE($\hat{Z}_H$) is computed for all four scan scenarios for five different times and three different elevation angles ($\sim$500 000 points). The effect of decreasing the number of samples on data quality is evident in Fig. 4, as the red curve—representing the histogram of RMSE values from

10 s PPIs—is clearly shifted to the right of the dark blue curve, representing the distribution of RMSE values from 20-s PPIs in CPS mode. This shows that the data quality is noticeably worse when the number of samples per radial has been decreased. The mean RMSE($\hat{Z}_H$) values for the set of $\sim$500 000 points are 1.77 (2.26) dBZ for PPIs collected over 20 (10) s, corresponding to a 28% increase in RMSE when the number of samples is reduced by a factor of 2. This is expected, as var($\hat{Z}_H$) is roughly inversely proportional to the number of pulses in (3). This difference in data quality can be seen qualitatively in Fig. 5, where additive white Gaussian noise (AWGN) has been added to each panel; the standard deviation of the AWGN is determined by the local standard deviation of Z_H. This is done in order to simulate the data that an actual radar would observe with each of the scanning strategies. When comparing Figs. 5a and 5b, Fig. 5b shows increased granularity and a ''coarser'' appearance (qualitatively) than Fig. 5a, indicating better data quality in Fig. 5a.

Next, BMX is analyzed as a scan speedup method. By qualitatively analyzing Fig. 3, there is clear spatial homogeneity in the PPI of RMSE($\hat{Z}_H$) values, reflected in the distinct histogram shape of BMX RMSE($\hat{Z}_H$) data (green curve in Fig. 4). A mathematical explanation of this phenomenon can

RMSE(v_r)

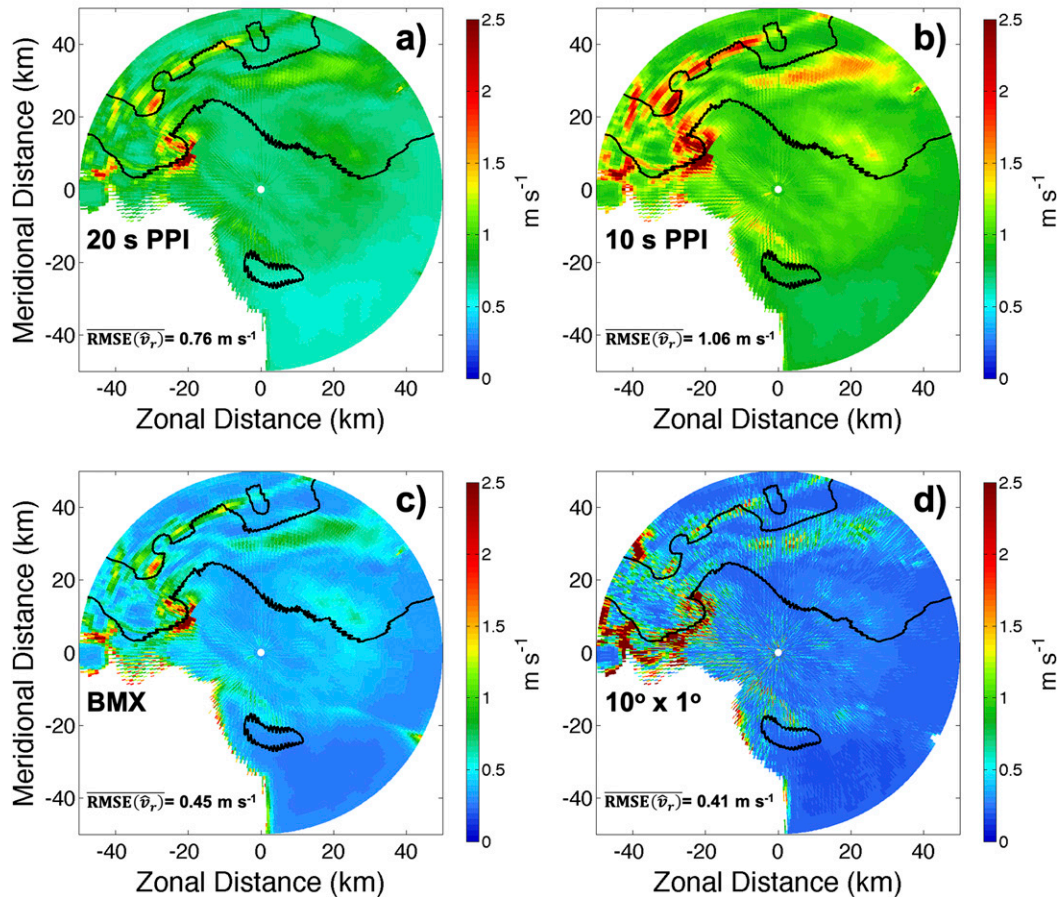
FIG. 8. As in Fig. 3, but for RMSE of v_r. RMSE values listed are the mean values from 15 PPIs. Note the qualitative similarity between the regions of high RMSE($\hat{v}_r$) and the regions of high spectrum width in Fig. 2c.

be derived by expanding all terms in (3) and (6) and making use of (6.12) in Doviak and Zrnić (1993):

$$\frac{1}{D_I} = \sum_{l=-D}^{D} \frac{D - |l| + 1}{D + 1} \rho^2(lT_s), \qquad (10)$$

where D_I is the total number of independent samples and all other variables are as defined in (3). Then, (3) and (6) can be separated into similar and dissimilar terms and values plugged in for $\rho(T_S)$ show that the range of error estimates yielded by (3) is wider than error estimates yielded by (6), especially at high SNR. This explains the difference in histogram shape between the BMX error estimates (green curve in Fig. 4) and all other histograms plotted in Fig. 4. For the collection of ~500 000 data points (example PPI in Fig. 3c), the mean RMSE($\hat{Z}_H$) is equal to 1.05 dBZ. This shows a significant improvement over the 1.77-dBZ mean RMSE($\hat{Z}_H$) value obtained for CPS, pencil-beam data collection in the 15 PPIs analyzed. The improvement in data quality is owed to the independence of pulse pairs in BMX data collection mode compared to CPS data collection mode.

Because (6) is inversely proportional to the number of samples, it is concluded that the expected mean RMSE($\hat{Z}_H$) is 1.48 dBZ when the scan time is reduced from 20 to 10 s per PPI. This number is calculated by multiplying the standard deviation of Z_H in BMX data collection mode by the square root of the difference in scan time ($\sqrt{2}$). Thus, it can be said that BMX can offer improved data quality, even in situations where the total scan time is decreased by a factor of 2. Working backward, the inverse proportionality between variance and number of samples can be leveraged to determine an "equivalent speedup factor." This corresponds to the factor by which the number of samples per radial can be reduced, while still maintaining the same data quality [as determined by mean RMSE($\hat{Z}_H$) of the NEXRAD-style scan]. For a comparison between RMSE($\hat{Z}_H$) for CPS and BMX, the speedup factor is equal to the ratio of mean RMSE($\hat{Z}_H$) squared. For this comparison, the equivalent speedup factor is $(1.77/1.05)^2 =$ 2.84. Thus, it can be said that when switching from CPS to BMX data collection mode, the scan time can be decreased by a factor of 2.84, while keeping data quality for Z_H constant.

Finally, radar imaging (10° azimuthal beam spoiling on transmit) is evaluated as a possible scan speedup method. Performing radar imaging while keeping the scan time constant (i.e., 20 s per PPI) increases the number of samples per radial, while decreasing the SNR at each point because of the reduction in incident power density; this was simulated by decreasing antenna gain on transmit, as antenna gain is directly proportional to the array aperture area [i.e., Eq. (12.7) in Skolnik 2008]. This has the effect of generally improving data quality in areas where there is minimal reflectivity gradient in the direction of beam spoiling, because in this area, the increase in the number of pulse pairs improves data quality more than higher two-way sidelobes and lower SNR reduce data quality. This can be calculated by using (3) but needs to be evaluated on a case-by-case basis as the effects on RMSE($\hat{Z}_H$) from changes in SNR, beam pattern changes, and the total number of pulses are nonlinear. This phenomenon is seen in Fig. 3d, where many of the estimates of RMSE($\hat{Z}_H$) are shown to be significantly improved (cyan colors in Fig. 3d), compared to Figs. 3a–c. However, there is a significant reduction in data quality around the edges of the supercell, especially to the southwest of the hook echo, where a sharp horizontal (i.e., parallel to beam spoiling direction) gradient in Z_H is present. A closer comparison of the horizontal Z_H gradient and the regions with high bias from radar imaging show that the bias to the south and southwest of the mesocyclone is collocated with—and is likely induced by—the sharp horizontal Z_H gradient in this region (Fig. 6). The gradient in Z_H is calculated by dividing the difference in Z_H between two surrounding points along a single range by the horizontal distance between the two points (i.e., dividing the Z_H difference between the $(i + 1)$ and the $(i − 1)$ radials at the same range gate by the horizontal distance between the two points). This results in very poor data quality [e.g., RMSE($\hat{Z}_H$) > 15 dBZ], because the values derived with the spoiled beam are biased with respect to the pencil beam due to higher sidelobes. This is represented by the dark red area on the western side of the PPI in Fig. 3d; the color bar in Fig. 3d is capped at 3 dBZ for consistency with the other panels in Fig. 3; some of the values in Fig. 3d exceed 15 dBZ. The histogram appears to show that radar imaging performs better than BMX for improving data quality (Fig. 4) but the area of extremely high RMSE($\hat{Z}_H$) values (not shown in Fig. 4) creates a situation where the mean RMSE($\hat{Z}_H$) is 1.17 dBZ, which is higher than that of BMX (1.05 dBZ). This underscores the point that radar imaging should be applied in an adaptive manner (e.g., Weber et al. 2017).

Based on mean RMSE($\hat{Z}_H$) alone, the speedup factor compared to a NEXRAD-type scan is 2.29 for radar imaging to 10° in azimuth. However, many meteorologists may find the regions with RMSE($\hat{Z}_H$) > 15 dBZ (caused by bias, in this case) to be unacceptable, despite the apparent "improvement" in data quality when simply considering the mean RMSE over the whole domain. Additionally, the loss in sensitivity that is apparent in Fig. 5d is a consideration, especially when trying to detect weak radar echoes such as developing precipitation, light precipitation, and fine-line features such as cold fronts and gust fronts.

For radar imaging, it is clear that the method does a good job of improving the data quality in the heavier precipitation cores
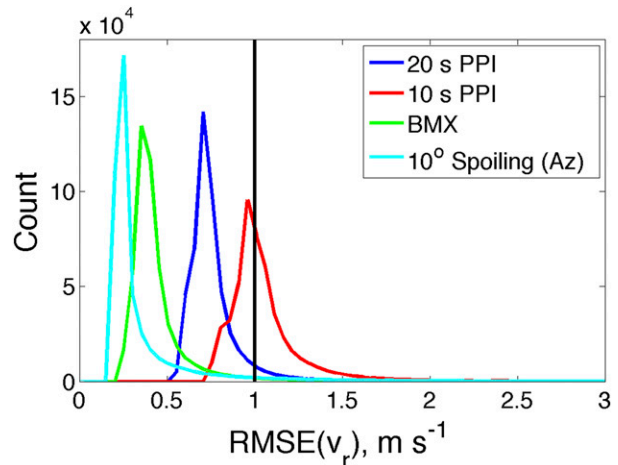

FIG. 9. As in Fig. 4, but for a histogram of v_r. The black vertical line represents the 1 m s^{-1} suggested requirement (see Table 2).

and away from large reflectivity gradients but creates a situation where data quality may be poor in regions near reflectivity gradients as a result of higher antenna sidelobes and where the loss of sensitivity reduces available data for forecasters. Thus, it is likely that the "best" method for utilizing radar imaging is to adaptively spoil the beam, in order to avoid spoiling across areas of sharp reflectivity gradients.

To assess whether or not the beamwidth of the radar (relative to the 1-km WRF grid spacing) affects the outcome of the scanning strategy comparison, the simulations plotted in Fig. 3 are rerun with a longer maximum radar range and a longer standoff range between the radar and the mesocyclone (Fig. 7). As can be seen by a qualitative comparison, the RMSE is essentially unchanged between Figs. 3 and 7. The discrepancy between the mean RMSE in Figs. 3d and 7d is largely due to the fact that in Fig. 7, there is a much larger region of low bias that lowers the mean RMSE($\hat{Z}_H$) for the domain of the new PPI. Thus, the results do not appear to change significantly as a function of range.

2) RADIAL VELOCITY (v_r)

In addition to analyzing the data quality impact on Z_H, this study also analyzes the impact on v_r using the same approach and methods described in section 3a(1). Again, data quality is compared between four scan strategies: 20-s PPIs with a pencil beam on transmit in CPS mode, 10-s PPIs with a pencil beam on transmit in CPS mode, 20-s PPIs with a pencil beam on transmit in BMX mode, and 20-s PPIs with a 10° azimuthally spoiled transmit beam in CPS mode.

The RMSE of $\hat{v}_r$ is calculated using (4), (7), and (9) for each scanning strategy; an example for one PPI per scan method is plotted in Fig. 8. Qualitatively, decreasing the scan time to 10 s (example in Fig. 8b) produces poorer data quality than for 20-s PPIs in CPS mode (Fig. 8a). For the collection of 15 PPIs, this corresponds to an increase in RMSE($\hat{v}_r$) from 0.76 to 1.06 m s^{-1}. (39% increase in RMSE; histogram shown in Fig. 9). The difference in data quality can be seen qualitatively in Fig. 10, where Fig. 10b appears to be noisier than
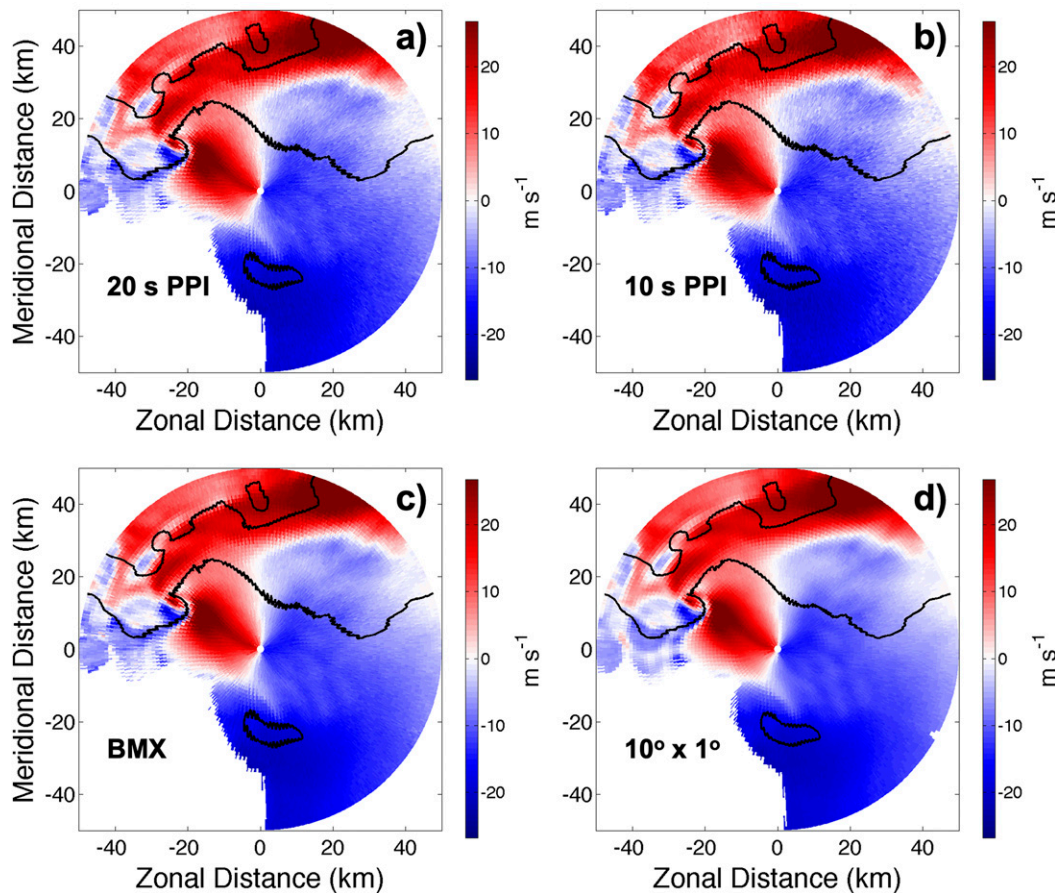
Radial Velocity (v_r)

FIG. 10. As in Fig. 5, but for v_r.

Fig. 10a. This phenomenon is most pronounced along and near the zero-isodop in the northeastern quadrant of the PPI.

By analyzing the distribution of the RMSE histogram in Fig. 9, it is also possible to compare the percentage of pixels that are of "acceptable" data quality under different scanning strategies. For the NEXRAD-style scan, 94.3% of pixels are of acceptable data quality for $\hat{v}_r$ [i.e., $\text{RMSE}(\hat{v}_r) < 1\,\text{m s}^{-1}$]. When the scan time is decreased from 20 to 10 s, the percentage of pixels with acceptable $\text{RMSE}(\hat{v}_r)$ estimates decreases to 49.5%. So, for a 10 s PPI collecting data in CPS mode, over half of the estimates of v_r are not acceptable—and nearly 45% of estimates change from acceptable to unacceptable when moving from 20-s PPIs to 10-s PPIs, based on the $1\,\text{m s}^{-1}$ requirement from the initial SENSR PPR (Federal Aviation Administration 2017).

Figure 8c plots $\text{RMSE}(\hat{v}_r)$ for a 20-s PPI where BMX mode is used. As expected, data quality is generally improved in BMX mode, compared with data quality in CPS mode. For all 15 PPIs analyzed in BMX mode, the mean $\text{RMSE}(\hat{v}_r)$ is $0.45\,\text{m s}^{-1}$; the corresponding histogram is plotted in Fig. 9. The equivalent speedup factor for BMX in this case is 2.85 when comparing the

mean $\text{RMSE}(\hat{v}_r)$ of the two scanning methods. In this case, it is also possible to calculate speedup factor based on the percentage of pixels in the domain with acceptable data quality. This is achieved by multiplying the RMSE estimates using BMX by the square root of the speedup factor [because the standard deviation of v_r is inversely proportional to the square root of the number of samples in (7)] and then calculating the percentage of pixels that have "acceptable" data quality. Using this method, BMX offers a speedup factor of 1.69 compared to CPS.

An interesting phenomenon that is present in Fig. 8c (BMX) that is not present in any of the other panels of this figure (or any panels in Fig. 3) is the relatively poor data quality (i.e., higher RMSE) around the periphery of the precipitation echo. Notably, the area along the edge of the storm (to the south and west of the radar) has worse data quality than in CPS mode, in Fig. 8a. This result is expected and is caused by the fact that the number of pulse pairs—and, by extension, the number of samples for estimation of v_r—is reduced by approximately a factor of 2 for BMX, compared to CPS. For example, a scan where 50 pulses per radial are transmitted would result in 50 Z_H samples in both CPS and BMX modes, 49 v_r samples in
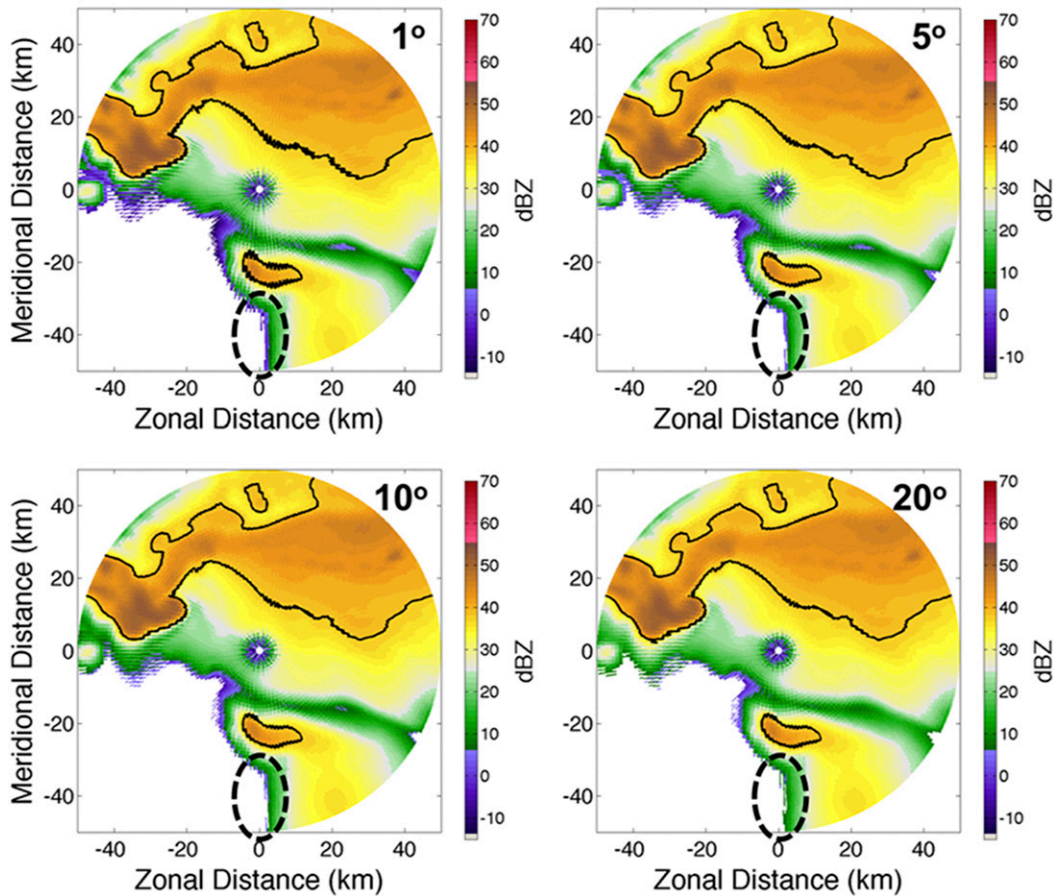
Reflectivity Factor (Z_H)

FIG. 11. Underlying Z_H reference fields for (top left) a pencil beam, as well as those for a beam spoiled by (top right) 5°, (bottom left) 10°, and (bottom right) 20° in azimuth. Note the loss in sensitivity as the amount of beam spoiling is increased (area surrounded by dashed oval in each panel).

CPS mode, but only 25 v_r samples in BMX mode, although all 25 v_r samples are entirely independent. If interpulse correlation $[\rho(T_S)]$ is low (as can be the case in low-SNR regions), then it is possible that CPS mode could yield more independent v_r samples than BMX mode. In this scenario, BMX data collection mode could produce poorer data quality than CPS data collection mode. This phenomenon corresponds to the portion of Fig. 1b for which the improvement factor is less than 1. However, this is dependent on several variables, including spectrum width and the number of pulses used, in addition to SNR. The reduction of v_r data quality in low-SNR environments may be mitigated by adaptive application of BMX in relatively high-SNR areas only.

Finally, the difference in data quality between a pencil beam and a 10° azimuthally spoiled beam is analyzed. In Fig. 8d, it is clear that most of the domain shows improved data quality when compared to the other three methods. However, there are regions of higher RMSE around the edge of the storm, especially to the south and west of the mesocyclone. Despite this area, the mean RMSE($\hat{v}_r$) for 10° of beam spoiling is

0.41 m s^{-1} (cyan curve in Fig. 9). The corresponding speedup factor is 3.44. However, as mentioned in section 3a(1), the higher two-way antenna sidelobes may produce regions where data quality is unacceptable for forecasters. This is exemplified by analyzing the percentage of pixels with acceptable data quality; as previously stated, the 20-s PPI with CPS data collection resulted in 94.3% of the pixels having acceptable data quality for v_r [i.e., RMSE($\hat{v}_r$) < 1 m s^{-1}]. For a 10° azimuthally spoiled transmit beam with all other scan parameters held constant, the percentage of "acceptable" pixels is 94.1%. As a result, no significant improvement in the percentage of pixels with acceptable RMSE($\hat{v}_r$) estimates can be found via radar imaging in azimuth, due to the introduction of bias from the higher two-way sidelobes.

One interesting feature in Fig. 8 compared to Fig. 3 is the relative RMSE in the areas of high spectrum width. In Fig. 3, RMSE($\hat{Z}_H$) tends to decrease in the areas of high spectrum width, such as those near the mesocyclone and inflow region of the supercell. This is because each estimate of Z_H is produced by a single pulse (i.e., a lag-0 estimator), such that decreased
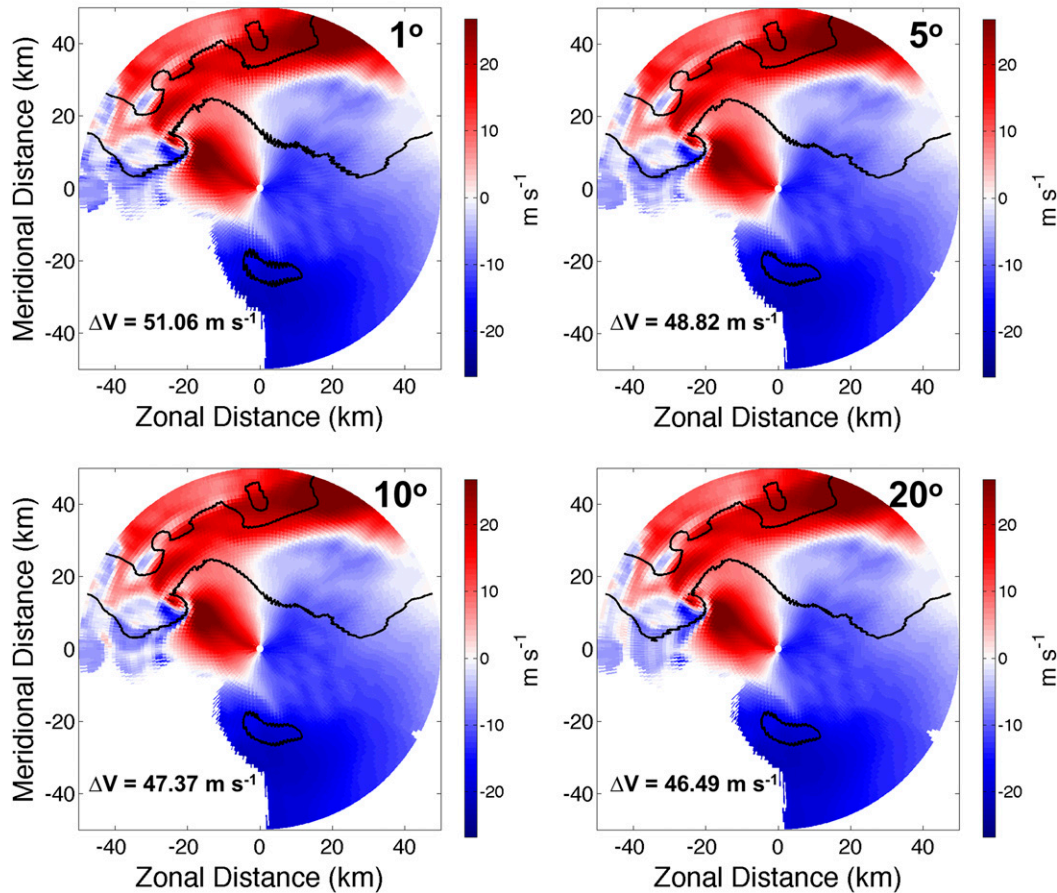
Radial Velocity (v_r)

FIG. 12. As in Fig. 11, but for v_r. The value for ΔV in each panel corresponds to the measured mesocyclone intensity with each amount of beam spoiling.

interpulse correlation within a pulse pair improves the number of independent samples, thereby improving data quality. For BMX, this is reflected mathematically in (6) by the fact that in the high-SNR limit, $\text{var}(\hat{S}_I)$ is directly proportional to $(1 + \rho^2(T_S))$, such that decreasing sample correlation decreases the expected statistical variance. Conversely, RMSE of $\hat{v}_r$ tends to increase in areas where spectrum width is larger. For the variance of radial velocity in (7), in the high-SNR limit, $\text{var}(\hat{v}_r)$ is proportional to $\{1/[\rho^2(T_S)] - 1\}$, such that decreasing interpulse correlation within a pulse pair increases the resulting variance. The increase in the number of independent samples is why data quality improves for Z_H in areas of high spectrum width but is degraded for v_r in areas of high spectrum width due to decreased interpulse correlation. A more complete mathematical explanation of this phenomenon can be found in Zrnić (1977).

b. Effect of radar imaging on mesocyclone intensity observations

To assess the impact that radar imaging has on observed mesocyclone intensity, PPIs of v_r with varying degrees and directions of beam spoiling have been simulated. The two-way beam pattern is simulated by multiplying a transmit beam of 1°, 5°, 10°, and 20° in azimuth (1° in elevation) by a narrow ($\sim$1° $\times$ 1°) receive beam. Each of the 4 two-way beam patterns are used to scan the mesocyclone. The mesocyclone strength is calculated by using ΔV, the difference between the maximum inbound and outbound v_r in the mesocyclone. This experiment is performed because of the potential for bias caused by radar imaging in areas with sharp Z_H or v_r gradients. Other techniques—such as BMX—should not have a systematic bias on the derived Z_H and v_r in this region because the beam pattern should remain the same.

The results of spoiling the transmit beam to 1°, 5°, 10°, and 20° in azimuth are shown in Figs. 11 and 12. As beam spoiling increases in the azimuthal direction, the measured ΔV begins to decrease; the calculated ΔV values are listed in each panel of Fig. 12. With a 1° pencil beam on transmit, the measured ΔV is 51.06 m s^{-1}. When transmit beam spoiling is increased, however, the measured ΔV value decreases. When spoiling by 20° on transmit, measured ΔV is 46.49 m s^{-1}. The 4.4%–9.0%

underestimation in mesocyclone intensity for 5°–20° of beam spoiling is caused by "smearing" of the velocity couplet signature, which can be thought of in similar terms to a low-pass filter. This effect can be observed in a radial velocity profile across several angles at a given range (Fig. 13). The magnitudes of the extrema are generally smaller for the cases with more beam spoiling (i.e., green curve in Fig. 13) compared to the pencil beam case (i.e., dark blue curve in Fig. 13). This agrees with Brown et al. (2002), where tornado detection capability is assessed under native and enhanced resolution for a simulated WSR-88D. The results from Brown et al. (2002) show that Doppler velocity signatures generally appear stronger when the azimuthal sampling is reduced from 1.0° to 0.5°. Our study is different, however, in that a full beam pattern is simulated for a notional phased array radar (i.e., wide beam on transmit and narrow beam on receive).

This procedure is also performed for 1°, 5°, 10°, and 20° of spoiling in the elevation dimension. The result for this supercell case is that the calculated ΔV values in and around the mesocyclone do not change appreciably when spoiling is increased in elevation (Fig. 14). It is hypothesized that this result is due to the fact that for this case, the primary Z_H gradients are in the azimuthal dimension, rather than the elevation dimension. While the result in this study indicates that spoiling in elevation may be favorable compared to spoiling in azimuth for correctly assessing mesocyclone strength, this is only one application of assessing the effect of radar imaging. This result may change for a different case, if stronger vertical gradients in Z_H are present. For example, the Atmospheric Imaging Radar (AIR; Isom et al. 2013) operates by transmitting a 1° × 20° (azimuth × elevation) beam; artifacts from vertical sidelobes and/or grating lobes have been shown in some datasets collected by the AIR (Kurdzo et al. 2017; Mahre et al. 2018).

4. Conclusions

a. Summary

In this study, data quality in and around a simulated supercell is assessed by using a large-domain weather radar simulator. This research is done in order to inform decisions about which scan speedup strategy (or combination of strategies) can provide the highest-quality data and is shown here for a prototypical high-impact weather event (tornadic supercell). The results of this study can be used to guide the design of VCPs for a NexPAR system and can be used to assess the expected data quality for various volumetric update times. Scanning strategies that show promise for achieving a rapid-scan timeline include BMX data collection mode and radar imaging.

One scan speedup method evaluated in this study is BMX. This method shows considerable promise for obtaining rapid-scan weather radar data with acceptable data quality. For RMSE($\hat{Z}_H$) and RMSE($\hat{v}_r$), it is shown that a speedup factor of 1.69–2.85 is achievable, such that the scan can be sped up by a factor of 1.69–2.85 without an increase in the mean RMSE($\hat{Z}_H$) or RMSE($\hat{v}_r$). This result is generally consistent with results in Yu et al. (2007), which posited that a speedup factor of 2–4 should be possible with BMX. The results of this study show
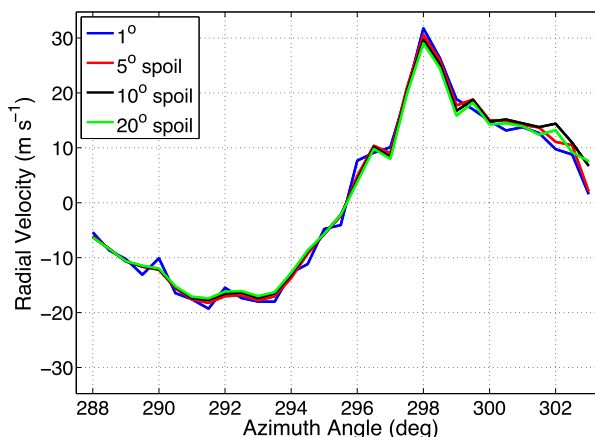

FIG. 13. The azimuthal radial velocity profile across the rotational couplet at 0.5° in elevation (approximately 300 m AGL). Note that increasing the beam spoiling factor tends to decrease the measured ΔV velocity shear.

significant promise for BMX as a viable option for meeting a rapid-scan timeline. While this technique must be used judiciously at low levels and in low-SNR regions—and is not compatible with staggered PRT data collection or ground clutter filtering—it generally offers a significant improvement in 1) data quality and 2) the time in which a full volume can be scanned without degrading data quality.

Additionally, radar imaging is shown to be a viable option for speeding up total volumetric update time. When calculating the speedup factor associated with a 10° azimuthally spoiled beam, each scan can be sped up by a factor of 2.29–3.44 (using mean RMSE value to be the metric for data quality). However, this does not fully capture the effects that a region of poor data quality might have on an operational forecaster. For example, the speedup factor reduces to approximately 1 when calculating the percentage of "acceptable" pixels between the two scan methods, such that no net gain is afforded. Additionally, regions of extremely biased [RMSE($\hat{Z}_H$) > 20 dBZ] data may be present and sensitivity to weak echoes is reduced. Thus, radar imaging should not be applied to an entire domain without first analyzing which areas are most susceptible to negative effects of radar imaging (i.e., areas with a strong reflectivity gradient). This is one area where adaptive scanning and/or cognitive radar may help to realize benefits of radar imaging. Because both BMX and radar imaging are most easily achievable with an all-digital phased array radar, the results presented in this study can help to inform decisions about possible radar architectures for a future NEXRAD replacement system.

Furthermore, the effects of radar imaging on the calculated mesocyclone strength are discussed for an example case. It is shown that for this case, the derived mesocyclone strength decreases as beam spoiling increases in azimuth. This result is expected and echoes results in Brown et al. (2002). An interesting result from this study is that the magnitude of change in derived ΔV is 4.4%–9.0% when spoiling in azimuth by 5° to 20°. Additionally, ΔV is calculated for 1°, 5°, 10°, and 20° of spoiling in elevation; for the case analyzed in this study, there is no
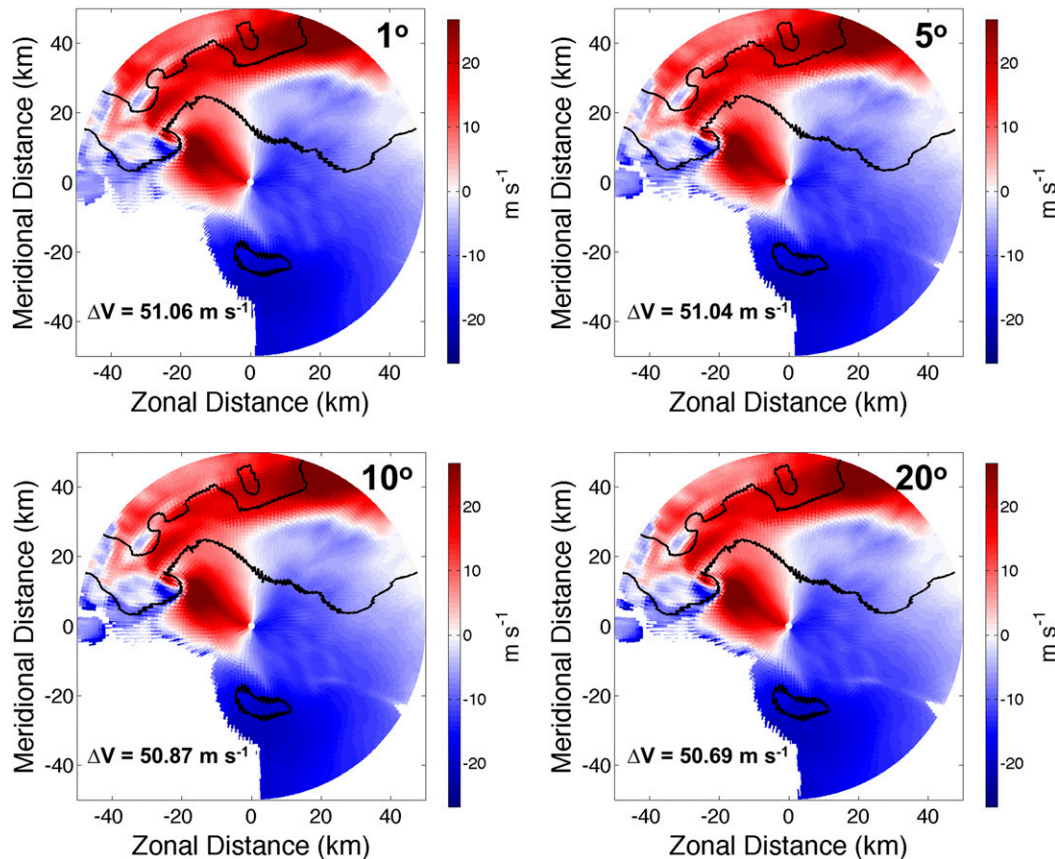
Radial Velocity (v_r)

FIG. 14. As in Fig. 12, but for spoiling in elevation, rather than azimuth.

appreciable effect on ΔV. It is believed that this is due to a lack of strong reflectivity gradients in the vertical dimension and the fact that the rotation (mesocyclone) is vertically aligned. Further testing should be conducted to assess whether this result is robust for many cases.

b. Future work

In the future, we plan to extend this study to cover adaptive scanning and its effects on data quality. One advantage of a fully digital phased array radar is the ability to control the location and shape of the radar beam. Controlling the radar beam location can allow for more pulses to be sent out along radials of interest, as fewer pulses are sent out along radials of lesser interest. Adaptive reallocation of receive beam clusters (adaptive radar imaging) has been explored in Weber et al. (2017) to speed up scans while minimizing effects on data quality from higher sidelobes on transmit. It would be a goal of such a study to adaptively reallocate pulses to improve data quality for a set scan time, or to maintain a certain level of data quality while decreasing scan time. Additionally, it would be beneficial to test these scanning strategies on an all-digital phased array radar system (i.e., Horus; Palmer et al. 2019) to

verify the simulated results and to compare simulated results to observed cases of various weather phenomena. This would be especially beneficial for assessing polarimetric data quality under various scanning conditions; polarimetric data quality is not considered in this study because the contributions of the phased array radar architecture to the expected radar variable errors could be larger than the contributions due to the statistical fluctuations alone. However, addressing the statistical fluctuations of polarimetric data is still an area which will have to be addressed for a NexPAR system in the future.

This study can also be expanded to other methods of scan speedup. For example, the multiple-beam technique (MBT) proposed in Zrnić et al. (2015) can be implemented under various conditions (varying the number of beams, the pulse length, etc.). Additionally, this framework can be used to compare the changes in expected data quality when pulse compression techniques are used to increase the number of independent samples in the along-range direction. Finally, this simulation framework can be applied to multiple meteorological events to evaluate if these findings are representative of scenarios beyond the supercell case considered in this study (e.g., different convective modes such as squall lines

or ordinary convection, flash flooding, and quantitative precipitation estimation).

REFERENCES

Bieringer, P., and P. S. Ray, 1996: A comparison of tornado warning lead times with and without NEXRAD Doppler radar. *Wea. Forecasting*, **11**, 47–52, https://doi.org/10.1175/1520-0434(1996)011<0047:ACOTWL>2.0.CO;2.

Bluestein, H. B., K. J. Thiem, J. C. Snyder, and J. B. Houser, 2018: The multiple-vortex structure of the El Reno, Oklahoma, tornado on 31 May 2013. *Mon. Wea. Rev.*, **146**, 2483–2502, https://doi.org/10.1175/MWR-D-18-0073.1.

——, ——, ——, and ——, 2019: Tornadogenesis and early tornado evolution in the El Reno, Oklahoma, supercell on 31 May 2013. *Mon. Wea. Rev.*, **147**, 2045–2066, https://doi.org/10.1175/MWR-D-18-0338.1.

Bodine, D. J., and K. L. Rasmussen, 2017: Evolution of mesoscale convective system organizational structure and convective line propagation. *Mon. Wea. Rev.*, **145**, 3419–3440, https://doi.org/10.1175/MWR-D-16-0406.1.

Brewster, K. A., and D. S. Zrnić, 1986: Comparison of eddy dissipation rate from spatial spectra of Doppler velocities and Doppler spectrum widths. *J. Atmos. Oceanic Technol.*, **3**, 440–452, https://doi.org/10.1175/1520-0426(1986)003<0440:COEDRF>2.0.CO;2.

Brooks, H. E., and J. Correia Jr., 2018: Long-term performance metrics for National Weather Service tornado warnings. *Wea. Forecasting*, **33**, 1501–1511, https://doi.org/10.1175/WAF-D-18-0120.1.

Brown, R. A., V. T. Wood, and D. Sirmans, 2002: Improved tornado detection using simulated and actual WSR-88D data with enhanced resolution. *J. Atmos. Oceanic Technol.*, **19**, 1759–1771, https://doi.org/10.1175/1520-0426(2002)019<1759:ITDUSA>2.0.CO;2.

Carbone, R. E., M. J. Carpenter, and C. D. Burghart, 1985: Doppler radar sampling limitations in convective storms. *J. Atmos. Oceanic Technol.*, **2**, 357–361, https://doi.org/10.1175/1520-0426(1985)002<0357:DRSLIC>2.0.CO;2.

Chen, F., and J. Dudhia, 2001: Coupling an advanced land surface-hydrology model with the Penn State–NCAR MM5 modeling system. Part I: Model implementation and sensitivity. *Mon. Wea. Rev.*, **129**, 569–585, https://doi.org/10.1175/1520-0493(2001)129<0569:CAALSH>2.0.CO;2.

Chrisman, J. N., 2009: Automated Volume Scan Evaluation and Termination (AVSET): A simple technique to achieve faster volume scan updates for the WSR-88D. *34th Conf. on Radar Meteor.*, Williamsburg, VA, Amer. Meteor. Soc., P4.4, https://ams.confex.com/ams/34Radar/webprogram/Paper155324.html.

Doviak, R. J., and D. S. Zrnić, 1993: *Doppler Radar and Weather Observations*. Dover Publications, Inc., 562 pp.

Dudhia, J., 1989: Numerical study of convection observed during the Winter Monsoon Experiment using a mesoscale two-dimensional model. *J. Atmos. Sci.*, **46**, 3077–3107, https://doi.org/10.1175/1520-0469(1989)046<3077:NSOCOD>2.0.CO;2.

Fang, M., R. J. Doviak, and V. Melnikov, 2004: Spectrum width measured by WSR-88D: Error sources and statistics of various weather phenomena. *J. Atmos. Oceanic Technol.*, **21**, 888–904, https://doi.org/10.1175/1520-0426(2004)021<0888:SWMBWE>2.0.CO;2.

Federal Aviation Administration, 2017: Spectrum Efficient National Surveillance Radar program (SENSR)—Formal request for information (RFI). FAA Rep., 55 pp., https://faaco.faa.gov/index.cfm/attachment/download/73825.

French, M. M., H. B. Bluestein, I. PopStefanija, C. A. Baldi, and R. T. Bluth, 2013: Reexamining the vertical development of tornadic vortex signatures in supercells. *Mon. Wea. Rev.*, **141**, 4576–4601, https://doi.org/10.1175/MWR-D-12-00315.1.

——, ——, ——, ——, and ——, 2014: Mobile, phased-array, Doppler radar observations of tornadoes at X band. *Mon. Wea. Rev.*, **142**, 1010–1036, https://doi.org/10.1175/MWR-D-13-00101.1.

Frisch, A. S., and R. G. Strauch, 1976: Doppler radar measurements of turbulent kinetic energy dissipation rates in a northeastern Colorado convective storm. *J. Appl. Meteor.*, **15**, 1012–1017, https://doi.org/10.1175/1520-0450(1976)015<1012:DRMOTK>2.0.CO;2.

Griffin, C. B., D. J. Bodine, J. M. Kurdzo, A. Mahre, and R. D. Palmer, 2019: High-temporal resolution observations of the 27 May 2015 Canadian, Texas, tornado using the Atmospheric Imaging Radar. *Mon. Wea. Rev.*, **147**, 873–891, https://doi.org/10.1175/MWR-D-18-0297.1.

Heinselman, P. L., and S. M. Torres, 2011: High-temporal-resolution capabilities of the National Weather Radar Testbed phased-array radar. *J. Appl. Meteor. Climatol.*, **50**, 579–593, https://doi.org/10.1175/2010JAMC2588.1.

——, D. S. LaDue, and H. Lazrus, 2012: Exploring impacts of rapid-scan radar data on NWS warning decisions. *Wea. Forecasting*, **27**, 1031–1044, https://doi.org/10.1175/WAF-D-11-00145.1.

Hong, S.-Y., Y. Noh, and J. Dudhia, 2006: A new vertical diffusion package with an explicit treatment of entrainment processes. *Mon. Wea. Rev.*, **134**, 2318–2341, https://doi.org/10.1175/MWR3199.1.

Houser, J. L., H. B. Bluestein, and J. C. Snyder, 2015: Rapid-scan, polarimetric, Doppler radar observations of tornadogenesis and tornado dissipation in a tornadic supercell: The "El Reno, Oklahoma" storm of 24 May 2011. *Mon. Wea. Rev.*, **143**, 2685–2710, https://doi.org/10.1175/MWR-D-14-00253.1.

Isom, B., and Coauthors, 2013: The Atmospheric Imaging Radar: Simultaneous volumetric observations using a phased array weather radar. *J. Atmos. Oceanic Technol.*, **30**, 655–675, https://doi.org/10.1175/JTECH-D-12-00063.1.

Jung, Y., G. Zhang, and M. Xue, 2008: Assimilation of simulated polarimetric radar data for a convective storm using the ensemble Kalman filter. Part I: Observation operators for reflectivity and polarimetric variables. *Mon. Wea. Rev.*, **136**, 2228–2245, https://doi.org/10.1175/2007MWR2083.1.

Kurdzo, J. M., and Coauthors, 2017: Observations of severe local storms and tornadoes with the Atmospheric Imaging Radar. *Bull. Amer. Meteor. Soc.*, **98**, 915–935, https://doi.org/10.1175/BAMS-D-15-00266.1.

Mahre, A., T.-Y. Yu, R. D. Palmer, and J. M. Kurdzo, 2017: Observations of a cold front at high spatiotemporal resolution using an X-band phased array imaging radar. *Atmosphere*, **8**, 30, https://doi.org/10.3390/atmos8020030.

——, J. M. Kurdzo, D. J. Bodine, C. B. Griffin, R. D. Palmer, and T.-Y. Yu, 2018: Analysis of the 16 May 2015 Tipton,

Oklahoma, EF-3 tornado at high spatiotemporal resolution using the Atmospheric Imaging Radar. *Mon. Wea. Rev.*, **146**, 2103–2124, https://doi.org/10.1175/MWR-D-17-0256.1.

Melnikov, V. M., R. J. Doviak, and D. S. Zrnić, 2015: A method to increase the scanning rate of phased-array weather radar. *IEEE Trans. Geosci. Remote Sens.*, **53**, 5634–5643, https://doi.org/10.1109/TGRS.2015.2426704.

Mishchenko, M. I., 2000: Calculation of the amplitude matrix for a nonspherical particle in a fixed orientation. *Appl. Opt.*, **39**, 1026–1031, https://doi.org/10.1364/AO.39.001026.

——, L. D. Travis, and D. W. Mackowski, 1996: T-matrix computations of light scattering by nonspherical particles: A review. *J. Quant. Spectrosc. Radiat. Transfer*, **55**, 535–575, https://doi.org/10.1016/0022-4073(96)00002-7.

Mlawer, E. J., S. J. Taubman, P. D. Brown, M. J. Iacono, and S. A. Clough, 1997: Radiative transfer for inhomogeneous atmospheres: RRTM, a validated correlated-k model for the longwave. *J. Geophys. Res.*, **102**, 16 663–16 682, https://doi.org/10.1029/97JD00237.

Nastrom, G. D., and F. D. Eaton, 1997: Turbulence eddy dissipation rates from radar observations at 5-20 km at White Sands Missile Range, New Mexico. *J. Geophys. Res.*, **102**, 19 495–19 505, https://doi.org/10.1029/97JD01262.

National Research Council, 1995: *Assessment of NEXRAD Coverage and Associated Weather Services.* National Academies Press, 112 pp., https://doi.org/10.17226/9056.

Orfanidis, S. J., 2016: *Electromagnetic Waves and Antennas.* Orfanidis, 1413 pp.

Palmer, R. D., C. J. Fulton, J. Salazar, H. Sigmarsson, and M. Yeary, 2019: The "Horus" radar: An all-digital polarimetric phased array radar for multi-mission surveillance. *35th Conf. on Environmental Information Processing Technologies*, Phoenix, AZ, Amer. Meteor. Soc., 8A.6, https://ams.confex.com/ams/2019Annual/webprogram/Paper349962.html.

Polger, P. D., B. S. Goldsmith, R. C. Przywarty, and J. R. Bocchieri, 1994: National Weather Service warning performance based on the WSR-88D. *Bull. Amer. Meteor. Soc.*, **75**, 203–214, https://doi.org/10.1175/1520-0477(1994)075<0203:NWSWPB>2.0.CO;2.

Reinoso-Rondinel, R., T.-Y. Yu, and S. Torres, 2010: Multifunction phased-array radar: Time balance scheduler for adaptive weather sensing. *J. Atmos. Oceanic Technol.*, **27**, 1854–1867, https://doi.org/10.1175/2010JTECHA1420.1.

Simmons, K. M., and D. Sutter, 2005: WSR-88D radar, tornado warnings, and tornado casualties. *Wea. Forecasting*, **20**, 301–310, https://doi.org/10.1175/WAF857.1.

Skamarock, W. C., and Coauthors, 2008: A description of the Advanced Research WRF version 3. NCAR Tech. Note NCAR/TN-475+STR, 113 pp., https://doi.org/10.5065/D68S4MVH.

Skolnik, M., 2008: *Radar Handbook.* McGraw-Hill Education, 1328 pp.

Sun, J., and Coauthors, 2014: Use of NWP for nowcasting convective precipitation: Recent progress and challenges. *Bull. Amer. Meteor. Soc.*, **95**, 409–426, https://doi.org/10.1175/BAMS-D-11-00263.1.

Supinie, T. A., N. Yussouf, Y. Jung, M. Xue, J. Cheng, and S. Wang, 2017: Comparison of the analyses and forecasts of a tornadic supercell storm from assimilating phased-array radar and WSR-88D observations. *Wea. Forecasting*, **32**, 1379–1401, https://doi.org/10.1175/WAF-D-16-0159.1.

Tanamachi, R. L., and P. L. Heinselman, 2016: Rapid-scan, polarimetric observations of central Oklahoma severe storms on 31 May 2013. *Wea. Forecasting*, **31**, 19–42, https://doi.org/10.1175/WAF-D-15-0111.1.

Wakimoto, R. M., N. T. Atkins, K. M. Butler, H. B. Bluestein, K. Thiem, J. Snyder, and J. Houser, 2015: Photogrammetric analysis of the 2013 El Reno tornado combined with mobile X-band polarimetric radar data. *Mon. Wea. Rev.*, **143**, 2657–2683, https://doi.org/10.1175/MWR-D-15-0034.1.

——, and Coauthors, 2016: Aerial damage survey of the 2013 El Reno tornado combined with mobile radar data. *Mon. Wea. Rev.*, **144**, 1749–1776, https://doi.org/10.1175/MWR-D-15-0367.1.

Weber, M. E., and J. S. Herd, 2019: Aperture size considerations for future operational phased array weather radar. *35th Conf. on Environmental Information Processing Technologies*, Phoenix, AZ, Amer. Meteor. Soc., 7A.4, https://ams.confex.com/ams/2019Annual/webprogram/Paper354075.html.

——, J. Y. N. Cho, and H. G. Thomas, 2017: Command and control for multifunction phased array radar. *IEEE Trans. Geosci. Remote Sens.*, **55**, 5899–5912, https://doi.org/10.1109/TGRS.2017.2716935.

——, J. Pica, C. D. Curtis, I. R. Ivic, D. Conway, and J. Y. N. Cho, 2019: Panel discussion: The next-generation operational weather radar network. *Phased Array Radar Symp.*, Phoenix, AZ, Amer. Meteor. Soc., PD1.1, https://ams.confex.com/ams/2019Annual/webprogram/Paper352287.html.

Wilson, K. A., P. L. Heinselman, C. M. Kuster, D. M. Kingfield, and Z. Kang, 2017: Forecaster performance and workload: Does radar update time matter? *Wea. Forecasting*, **32**, 253–274, https://doi.org/10.1175/WAF-D-16-0157.1.

Wolfson, M. M., and C. A. Meuse, 1993: Quantifying airport terminal area weather surveillance requirements. Preprints, *26th Int. Conf. on Radar Meteorology*, Norman, OK, Amer. Meteor. Soc., 47–49.

Wurman, J., and K. Kosiba, 2013: Finescale radar observations of tornado and mesocyclone structures. *Wea. Forecasting*, **28**, 1157–1174, https://doi.org/10.1175/WAF-D-12-00127.1.

——, ——, P. Robinson, and T. Marshall, 2014: The role of multiple-vortex tornado structure in causing storm researcher fatalities. *Bull. Amer. Meteor. Soc.*, **95**, 31–45, https://doi.org/10.1175/BAMS-D-13-00221.1.

Yu, T.-Y., M. B. Orescanin, C. D. Curtis, D. S. Zrnić, and D. E. Forsyth, 2007: Beam multiplexing using the phased-array weather radar. *J. Atmos. Oceanic Technol.*, **24**, 616–626, https://doi.org/10.1175/JTECH2052.1.

Yussouf, N., and D. J. Stensrud, 2010: Impact of phased-array radar observations over a short assimilation period: Observing system simulation experiments using an ensemble Kalman filter. *Mon. Wea. Rev.*, **138**, 517–538, https://doi.org/10.1175/2009MWR2925.1.

Zhang, G., J. Vivekanandan, and E. Brandes, 2001: A method for estimating rain rate and drop size distribution from polarimetric radar measurements. *IEEE Trans. Geosci. Remote Sens.*, **39**, 830–841, https://doi.org/10.1109/36.917906.

——, R. J. Doviak, D. S. Zrnić, R. Palmer, L. Lei, and Y. Al-Rashid, 2011: Polarimetric phased-array radar for weather measurement: A planar or cylindrical configuration? *J. Atmos. Oceanic Technol.*, **28**, 63–73, https://doi.org/10.1175/2010JTECHA1470.1.

Zhang, P., P. W. Chan, R. Doviak, and M. Fang, 2009: Estimate of the eddy dissipation rate using spectrum width observed by the Hong Kong TDWR radar. *Proc. 34th Conf. on Radar Meteorology*, Williamsburg, VA, Amer. Meteor. Soc., P6.9, https://ams.confex.com/ams/34Radar/techprogram/paper_155531.htm.

Zrnić, D. S., 1977: Spectral moment estimates from correlated pulse pairs. *IEEE Trans. Aerosp. Electron. Syst.*, **AES-13**, 344–354, https://doi.org/10.1109/TAES.1977.308467.

——, V. M. Melnikov, R. J. Doviak, and R. Palmer, 2015: Scanning strategy for the multifunction phased-array radar to satisfy aviation and meteorological needs. *IEEE Geosci. Remote Sens. Lett.*, **12**, 1204–1208, https://doi.org/10.1109/LGRS.2014.2388202.